# Mn promoted Co catalysts for Fischer-Tropsch production of light olefins - An experimental and theoretical study

Eirik Østbye Pedersen*[1], Ingeborg-Helene Svenum[2] and Edd A. Blekkan[1]

[1]Department of Chemical Engineering, Norwegian University of Science and Technology, 7491 Trondheim, Norway
[2]SINTEF Materials and Chemistry, 7465 Trondheim, Norway
*Corresponding author: eirik.o.pedersen@ntnu.no*

November 26, 2017

## Abstract

Three different CoMn/γ-$Al_2O_3$ catalysts were prepared by the incipient wetness impregnation route and compared to a Co/γ-$Al_2O_3$ catalyst. The effect of co-impregnation vs. sequential impregnation as well as the order of component addition was investigated. All catalysts were characterised by TPR, $H_2$-chemisorption, XRD and XPS and their activity and selectivity in the Fischer-Tropsch reaction was investigated. Complementary, self-consistent DFT calculations were performed to further address the observed promotion effects. All Mn promoted catalysts displayed heightened intrinsic activity, heightened selectivity to light olefins and $C_{5+}$ species and lowered selectivity to $CH_4$ compared to Co. The promotion effects on selectivity and intrinsic activity were found to be independent on catalyst preparation method. The catalysts undergo a restructuring during operation, in which an excess of Mn saturates the catalytically relevant sites causing the similar behaviour. The Co-specific activity differed between the Mn promoted catalysts. This was attributed to varying degrees of Mn incorporation in the $Co_3O_4$ particles, causing different degrees of reduction limiting the available metallic Co surface area. The DFT calculations suggested that the binding energy for all investigated species increases on Co in the presence of Mn, facilitating CO dissociation which can explain the higher intrinsic activity. The affected selectivities for olefins, $C_{5+}$ and $CH_4$ can all be attributed to an inhibited hydrogenation activity demonstrated by the increased barriers for $CH_3$ and $CH_4$ formation.

# 1 Introduction

Light olefins are among the most important chemical intermediates in the production of plastics, fibres and other organic chemicals. In 2011, the production of ethylene and propylene was 127 and 70 MT respectively, and the demand for both is projected to grow by 3.3 and 4.4 %/year, respectively [1]. Ethylene is produced mainly by steam cracking of natural gas and naphtha which carries a high capital investment cost. Propylene is primarily a by-product in ethylene plants and in fluid catalytic crackers used for gasoline production. Due to the increasing demand of propylene and a shifted focus towards higher ethylene selectivity in steam crackers, the gap between conventional propylene supply and demand is expected to grow. Consequently, there has been a growing interest towards alternative, on-purpose production of light olefins in both industry and academia [2].

Among the proposed alternative routes, the Fischer-Tropsch synthesis (FTS) process presents a potential option. As a synthesis gas process, it is highly flexible with respect to its source of carbon (coal, biomass, natural gas) in comparison to e.g. propane dehydrogenation. Compared to the other proposed syngas processes, (methanol to olefins, lower alcohol dehydration, cracking of FTS liquids) it presents a potential advantage as it is the only process that can convert syngas to olefins in one reaction step.

The FTS process produces hydrocarbons from synthesis gas ($CO + H_2$) by a chain-growth polymerisation process. Depending on the synthesis gas precursor, impurities and $H_2/CO$ ratio the preferred catalysts are either Fe or Co based. Conventionally, the hydrocarbons produced can be used as chemical intermediates or high purity fuels. More recently, it has been shown that high selectivity to light olefins is obtainable through tailored catalysts and specialised operation conditions. Fe based catalysts are the most frequently employed for this purpose, with high selectivity towards light olefins reported coupled with a low selectivity towards methane [2,3]. Cobalt catalysts are known for their high activity, may also provide high olefin selectivities, and is the preferred choice for synthesis gas with high $H_2$:CO ratio [4–7].

FTS products are to a large extent produced in accordance with the Anderson–Schulz–Flory (ASF) distribution. To increase the yield of light products, a higher temperature and lower pressure than conventional is applied. This has the drawback of also increasing the selectivity towards methane, which is the least desirable product in the FTS product range. Manganese is in both Co and Fe based FTS a frequently reported promoter for increasing olefin selectivity [2]. The experimental investigations into the promotion effect of Mn have been significant. As a general trend, in addition to increasing the olefin selectivity, Mn is in Co based FTS catalysts

reported as to increase catalyst activity, Co dispersion, $C_{5+}$ selectivity and to decrease $CH_4$ selectivity [8]. However, with different support materials, pre-treatments, Mn:Co ratios and preparation methods, reported results are also ranging from Mn having no discernible effects [9] to activity effects only [10] and to negative effects [4,11]. From the experimental data available, it is clear that the promotion effect of Mn is not fully understood, and strongly depends on the state and location of Mn with respect to Co, which again depends on preparation method, support etc.

While the experimental efforts to investigate the Co-Mn catalyst system have been substantial, the efforts from a theoretical point of view are limited. While there have been a significant number of theoretical investigations into FTS [12–14], the majority of the works focus on the much debated reaction mechanism [15–17], geometric effects [18–20] and the complicated selectivity scheme [21–24]. A few works exist on promotion with noble metals [25, 26] and boron [27]. Cheng et al. [28] investigated transition metal promotion, Mn included, and found only late transition metals to be likely olefin promoters, disagreeing with the experimental work. The need for an investigation on the promotion effect of Mn combining experimental and theoretical methods seems evident.

In the present work, the effects of Mn on Co based FTO are investigated by a combination of experimental and theoretical methods in order to further elucidate the nature of Mn promotion. In the experimental part, Mn promoted $Co/Al_2O_3$ catalysts are prepared, characterised and tested at industrially relevant FTS conditions favouring light olefin formation. The effect of preparation procedure, i.e. co-impregnation vs. sequential impregnation, is investigated as well as the order of component addition.

DFT calculations are performed where adsorption energies of relevant species as well as elementary reaction barriers are evaluated on clean and Mn modified Co(111) model surfaces. While *in situ* studies have found the operating state of Mn to be MnO [29], this work employs a simplified model where $Mn^{(0)}$ is considered in a surface alloy with Co.

# 2 Methods

## 2.1 Experimental

### 2.1.1 Catalyst Synthesis

All catalysts investigated were prepared by the incipient wetness impregnation (IWI) method using $Co(NO_3)_2 \cdot 6H_2O$ and $Mn(NO_3)_2 \cdot 4H_2O$ as precursors and γ-$Al_2O_3$ ($S_{BET}$ = 175 $m^2/g$) as the support material. The catalysts were dried overnight under reduced pressure and calcined in flowing air at 300 °C (2 °C/min) for 16 h. Prior to further characterisation and testing, all catalysts were sieved to a particle size of 53-90 μm.

Three $CoMn/Al_2O_3$ catalysts were prepared in addition to $Co/Al_2O_3$ to serve as the Co reference. Of the three CoMn catalysts, one was prepared in one step, hereafter referred to as Co+Mn, and two were prepared in two steps, one with Co followed by Mn (Co→Mn) and one with Mn followed by Co (Mn→Co). For all catalysts the Co loading was kept constant at 15% with respect to $Co+Al_2O_3$ and the Mn:Co ratio was kept at 1:4 w/w. For the sequentially impregnated catalysts, it was assumed that Co and Mn were present as $Co_3O_4$ and $MnO_2$ respectively after the first step [30]. For characterisation purposes, a fifth 3.75% $Mn/Al_2O_3$ sample without Co was also prepared.

### 2.1.2 Temperature Programmed Reduction

Temperature Programmed Reduction (TPR) was performed using an Altamira Instruments BenchCAT™ Hybrid instrument. The sample (0.15 g) was inserted into a 4 mm i.d. quartz U-tube reactor between two plugs of quartz wool. Pre-treatment consisted of heating in Ar flow (50 mL/min) to 300 °C (10 °C/min) for 30 min. Reduction took place in 50 mL/min 10% $H_2$/Ar flow, heating from ambient temperature to 800 °C (10 °C/min). The effluent gas was passed through a Drierite™ filled trap, to extract moisture before being passed over a thermal conductivity detector (TCD). To estimate the degree of reduction (DoR), the catalysts were reduced *in situ* by heating to 350 °C (1 °C/min) for 16 h in 25/25 mL/min $H_2$/Ar flow. The reduced catalysts were then cooled to 50 °C before being subjected to the same TPR procedure described above. The TPR profiles for the pre-reduced and calcined catalysts were integrated and compared. It was assumed that full $Co_3O_4 \rightarrow Co^{(0)}$ and $MnO_2 \rightarrow MnO$ reduction took place in the calcined samples and that only $CoO \rightarrow Co^{(0)}$ reduction took place in the pre-reduced samples.

### 2.1.3 $H_2$-Chemisorption

Volumetric $H_2$-chemisorption was performed using a Micromeritics ASAP 2020C instrument. The sample (0.3 g) was placed into a 9 mm i.d. quartz u-tube reactor between two plugs of quartz wool. The sample was reduced *in situ* in $H_2$ flow for 16 h at 350 °C (1 °C/min) before being cooled under vacuum. Chemisorption data was gathered at 40 °C at 15-507 mmHg $H_2$. The data between 100 and 507 mmHg were used to extrapolate and estimate the monolayer. For estimation of the dispersion, it was assumed that $H_2$ chemisorbs dissociatively and one H atom occupies one Co surface atom.

### 2.1.4 X-Ray Photoelectron Spectroscopy

X-ray photoelectron spectroscopy (XPS) was performed on a Kratos AXIS Ultra DLD instrument using a monochromated Al Kα X-ray source. The samples were mounted by pressing onto carbon tape. The equipment base pressure was in the range of $2\text{-}5 \cdot 10^{-9}$ Torr during acquisition. Measurements were done with take-off angle normal to the surface and individual core level spectra were recorded at a pass energy of 40 eV. Low energy electrons were used for charge compensation. Reported binding energies are referenced to the C 1s peak of adventitious carbon at 284.8 eV, resulting in an Al 2p contribution of $Al_2O_3$ at 72.3 eV.

### 2.1.5 X-Ray Diffraction

X-ray diffraction experiments (XRD) were performed at ambient temperature on a Bruker D8 Advance DaVinci X-ray diffractometer using a Cu Kα X-ray source. $Co_3O_4$ lattice constants and average particle sizes were obtained using the Pawley method [31] of full pattern fitting in the Topas 5.0 software [32]. A separate scan and fit of the γ-$Al_2O_3$ pattern was obtained and used in the refinement of the supported catalysts. Refinements were obtained with $R_{wp}$ values of approx. 4.2 %. Mn species were excluded from the refinement due to a very weak signal. The Co particle size was corrected for contraction during reduction by $d_{Co}^{(0)} = 0.75 \cdot d_{Co_3O_4}$ [33] and Co dispersion was then estimated by assuming spherical, uniform Co particles with site density of 14.6 atoms/nm$^2$ and using the formula D = 96/d, where D is Co dispersion (%) and d (nm) is average particle diameter [33].

### 2.1.6 Fischer-Tropsch Synthesis

Fischer-Tropsch Synthesis was performed in a 10 mm i.d. tubular stainless steel fixed bed reactor at 240-270 °C, 5 bara and $H_2/CO$ = 2.1. The catalyst (1 g) was diluted with inert SiC (19 g) to minimise temperature gradients and loaded into the reactor between plugs of quartz wool to keep the catalyst bed in place. The reactor was fixed in an aluminium block to further facilitate heat distribution and mounted in an electrical furnace.

The catalysts were reduced *in situ* in 125/125 mL/min $H_2$/He at 350 °C (1 °C/min) for 16 h. Subsequently, the reactor was pressurised in He flow to 5 bar at 180 °C before syngas (250 mL/min) was introduced. The reactor was then heated to 230 °C (20 °C/h) and 240 °C (5 °C/h). Effluent gases were passed through a hot trap kept at approx. 100 °C and a cold trap at ambient temperature before the gas phase was analysed by an Agilent Technologies 6890N GC fitted with a TCD and an FID. The syngas contained 3 % vol. $N_2$ which served as the GC internal standard. The space velocity or temperature was changed at 24 h intervals to reach set conversion levels. After the reaction, the reactor was cooled to ambient temperature in He flow and the catalyst was passivated in 0.5% $O_2/N_2$ flow for 2 h.

### 2.1.7 Catalyst Dewaxing

After passivation, the spent catalyst was extracted from the reactor and dewaxed by Soxhlet extraction. The wax containing catalyst and SiC mixture was placed in a cellulose thimble which was mounted in the main chamber of the Soxhlet extractor. The extractor was placed on an RB flask containing approx. 200 mL of xylene which was heated to 130-140 °C to reflux. The extraction process was run for approx. 48 h for multiple extraction cycles. The dewaxed catalyst was dried at 100 °C and magnetically separated from the SiC.

## 2.2 DFT Calculations

Self-consistent, spin polarised DFT calculations were performed using the Vienna *ab initio* simulation package (VASP) code [34–37]. The GGA-PBE [38, 39] functional was employed using 1st order Methfessel-Paxton electron smearing. The electron–ion interactions were described by the PAW [40, 41] method with a plane-wave cutoff energy of 500 eV. The Brillouin zone was sampled by a 7×7×1 Monkhorst–Pack grid [42]. The structures were optimised with a force criterion of 0.01 eV/Å. Transition states were

obtained by initially applying the climbing image nudged elastic band (CI-NEB) method [43,44], and further optimising using the Dimer method [45]. Transition states were confirmed by vibrational analysis yielding one imaginary frequency.

Three model systems, shown in Fig. 1, a Co surface and two Mn-modified Co surfaces oriented in the (111) direction were chosen. For the Mn-modified surfaces, Mn was added as a subsurface monolayer (Co/Mn/Co) and as a top monolayer (Mn/Co). Co can inhabit both the hcp and fcc phase, but in the case of $H_2$ activated Co, the fcc phase is most prominent [46]. Mn inhabits the I-43m space group, similar to the bcc structure [47], but is considered in a surface alloy with Co for the purpose of this work. The systems were modelled as a 5-layer slab and (2×2) surface unit cell. The three top layers were relaxed without restrictions during structural optimisations while the bottom two layers were fixed to the bulk lattice structure. An optimised bulk lattice parameter of 3.517 Å was obtained, in reasonable agreement with the experimental value of 3.545 Å [48] and used for the modelling of the slabs. The slabs were separated in the z-direction by a vacuum layer equivalent to 9 atomic layers.

# 3 Results and Discussion

## 3.1 Catalyst Characterisation

### 3.1.1 Temperature Programmed Reduction

Temperature programmed reduction profiles are shown in Fig. 2, with peak temperatures listed in Table 1. Three peaks were observed during the experiments. The first peak, appearing at about 190-230 °C, is most prominent for the Co and Co+Mn catalysts. This peak is reportedly caused by residual nitrates after calcination [33] and is consequently less prominent in Co→Mn and Mn→Co as they were calcined twice. The two latter peaks appear at about 290-330 and 410-550 °C respectively. These peaks originate from the stepwise reduction of $Co_3O_4$ [50]. Comparing the CoMn catalysts to the Co and Mn references, Mn has a significant effect on the catalyst reducibility. The Mn→Co catalyst appears very similar to Co, indicating slow or little Mn reduction. In the Co→Mn catalyst, the first peak is shifted to a higher temperature and has a higher intensity. It appears similar to the Co and Mn references superimposed on each other, indicating a delayed reduction of $Co_3O_4$ with simultaneous reduction of Mn. The Co+Mn profile shows evidence of strong Co↔Mn interaction with a significant increase in reduction temperature and broadening of the third peak. CoMn catalysts have previously been reported to form a

$Co_{3-x}Mn_xO_4$ type mixed oxide which remain in oxidic state during operation [29, 30, 51, 52]. The reduction of this oxidic phase is the probable cause of the significant broadening of the high temperature peak.

### 3.1.2 X-Ray Photoelectron Spectroscopy

XPS analysis were performed on the fresh (calcined) as well as spent (dewaxed) catalysts. The acquired Co 2p and Mn 2p core level spectra are shown in Fig. 3, with the corresponding Mn:Co, Co:Al, Mn:Al and (Mn+Co):Al atomic ratios listed in Table 2.

The Mn:Co atomic ratio is highest for the Co→Mn and lowest by Mn→Co, while in between for Co+Mn. This indicates that Mn is closely associated with Co, and that the second added phase covers the first, whereas a mixture exists for the co-impregnated sample. This is supported by Co:Al ratios, where the highest ratio is observed for Mn→Co and the lowest for Co→Mn. Interestingly, the Mn:Al ratio of the Mn reference is higher than the (Co+Mn):Al ratios for all the other catalysts. This indicates that Mn forms a highly dispersed phase over the $Al_2O_3$ when impregnated alone. When Co is added, both Mn:Al and (Co+Mn):Al ratios decreases, showing that Mn's affinity for Co is greater than its affinity for $Al_2O_3$.

The fresh catalysts show Co 2p peak shapes similar to what is reported for $Co_3O_4$ [53] and previously reported for supported Co catalyst [54]. The Co 2p spectra of the Co reference sample were fitted using the same fitting parameters determined by Biesinger et al. [53] for $Co_3O_4$. The FWHM values were allowed to increase during fitting due to the higher pass energy applied here. The peak position of the low binding energy contribution is at 779.6 eV agree well with the literature [53]. The CoMn catalysts display similar peak shape and binding energies. However, the fit is less optimal (not shown) when applying the same fitting parameters to the CoMn catalysts as the Co reference. This is probably due to changes caused by Co-Mn interactions. The Mn reference sample has a peak shape similar to that previously reported for $MnO_2$ [53], but is shifted about towards lower binding energies by about 0.4 eV. The Mn 2p spectra of the Mn promoted Co catalysts are different compared to the Mn reference, and appears more like $Mn_2O_3$ [53], but the signal to noise ratio is too low to make a conclusive remark. The Mn 3s spectra, while measured, were found too low to observe any 3s splitting and make an assessment of the oxidation state of Mn.

Both the Co 2p and Mn 2p core level changes for the spent catalysts compared to its fresh counterpart. The most distinct change is the increase at the high binding energy side of the

main feature in both spectra. These features are associated with satellite peaks and the overall peak shapes typically observed for CoO and MnO, respectively [53]. The Co 2p core levels of the Co reference and Mn promoted catalysts are somewhat different in overall shape compared to the CoO literature spectra [53]. The main low binding energy peak is at 780.5 eV. This is likely due to a different oxidation state of Co, e.g. $CoO_x$ or a mixed phase.

The Mn promoted catalysts exhibit a significant increase in the Mn:Co atomic ratio from before to after reaction, except for the Co→Mn. This suggests that Mn enriches to Co particle surface during reduction and/or FTS operation. This effect is largest for the Mn→Co catalyst where Mn is covered by Co after preparation, and negligible for the catalyst with Mn added last. Previously, Morales et al. [29] observed a similar trend from before to after reduction and attributed this to MnO segregating from the Co, decorating the support during reduction and forming a mixed oxide phase with the $TiO_2$. This is indicated as they observed Mn:Ti XPS ratios well above the bulk composition suggesting a highly dispersed Mn phase. Apart from for the Mn reference, this is never observed in our work. Moreover, the TPR profiles indicate that Mn is associated with Co at temperatures well above the reduction temperature. It seems more likely that Mn remains closely associated with Co during operation, but the Co surface gets enriched with Mn during operation. Using carbon nanofibres (CNF) as support material, Bezemer et al. [55] did not observe any segregation from before to after reduction. CNFs, due to their chemical inertness and weak metal-support interaction are extensively used as model support materials in FTS to investigate isolated effects [56–60]. It would appear Co-Mn segregation is less severe on $\gamma$-$Al_2O_3$ and CNF than for a strongly interacting support like $TiO_2$.

A more surprising result is the substantial (up to 3-fold) increase observed in the Co:Al ratios from before to after reaction. The previously mentioned work [29] observes a mild increase for CoMn catalysts during reduction and attributes this to the segregation effect. As we also observe this for an unpromoted Co catalyst, Mn segregation onto the support cannot explain this alone. Previous investigations [61, 62] have revealed that Co particles may break up and form a highly dispersed phase after reduction-oxidation-reduction treatment. As the catalysts investigated here are reduced, then passivated and heated during Soxhlet extraction and drying, a similar effect may be the cause of the observed increase in Co:Al ratios.

### 3.1.3 Dispersion

Measured dispersions and particle sizes are shown in Table 1 without the Mn reference which did not adsorb $H_2$. For the $H_2$-chemisorption measured dispersions, significant differences are observed between samples with results ranging from 2.2 to 5.5 %. All Mn-promoted catalysts show lower dispersions than the unpromoted catalyst. In comparison, the particle sizes and dispersions based on XRD show very little variation indicating that the differences in $H_2$ uptake/$Co^{(0)}$-surface area are not caused by differing Co particle sizes. Two alternative explanations are blockage of Co sites by Mn, or a partially oxidised Co surface. If blockage by Mn were the principal cause of the diminished $Co^{(0)}$ surface it would have been expected that the Co→Mn catalyst, rather than the Co+Mn catalyst exhibited the lowest dispersion, both by considering the preparation method and the observed Mn:Co XPS signal ratios. A much better correlation is observed between the measured DoR and the observed $H_2$-chemisorption measured dispersions. A weakness worth noting with this method of DoR estimation is that is does not differ between reduced and irreducible Co. At high temperatures, Co is known to migrate into the γ-$Al_2O_3$ lattice [63] and become irreducible, which would cause an overestimation of the DoR. Observing the XRD patterns shown in Fig. 4, a weak $MnO_2$ signal is visible at 28.7, 44.8 and 55.7°. This is clearest in the Co→Mn and Mn→Co, indicating two separate Co and Mn phases. Whereas for Co+Mn, the signal corresponding to $MnO_2$ is less apparent suggesting that Mn is to a larger extent incorporated in the $Co_3O_4$ particles. This is also supported by the estimated lattice parameters (Table 1) where lattice expansion of $Co_3O_4$ is observed for all Mn promoted samples indicating at least some degree of Mn incorporation in the $Co_3O_4$ lattice [64]. As shown earlier, this has a pronounced effect on the reducibility. However, the correlation between the degree of Mn incorporation and dispersion is less apparent, with the Mn→Co catalyst, which has the highest dispersion of the Mn promoted catalysts displaying the 2$^{nd}$ highest lattice expansion. This catalyst also has the lowest Mn:Co XPS signal ratio both before and after reaction, so it is possible the unreduced $Co_{3-x}Mn_xO_4$ is situated further from the surface and having less of a limiting effect on the dispersion. Consequently, different degrees of partial reduction of the catalyst surface is likely the main cause of the observed differences in dispersion.

This correlation between Mn promotion and lowered reducibility and dispersion is consistent with what has been seen in previous studies [10, 30]. However, it has been found that small amounts of Mn may have a beneficial effect on dispersion [65]. This was attributed to Mn forming a mixed compound with the support ($TiO_2$) and inhibiting strong metal-support interactions (SMSI) effects with Co. Increasing the amount of Mn resulted in a lowered dispersion agreeing with our results. Of course, an SMSI effect is not

expected with $Al_2O_3$ as the support, which in combination with our comparably high Mn loading explains why no such effect is seen here.

### 3.2 Fischer-Tropsch Synthesis

The CO conversion and site-time yields for the catalysts in the initial 24 h of operation are shown in Fig. 5. The catalyst performances vary from 20-45 % CO conversion. Observing the intrinsic activity, it can be seen that all Mn-promoted catalysts exhibit site-time yields approximately 50 % higher than the unpromoted catalyst. For the initial 2-4 h, this behaviour appears to be independent on the preparation method, suggesting that the differences in conversion between the Mn-promoted catalysts are primarily caused by the observed differences in available Co surface area. It has previously been suggested that Mn decorates the Co particle surfaces and that the source of its promoting effect is enhanced activity sites near the Co-Mn interface [66]. Our XPS results, which show a surface enrichment of Mn from before to after operation is not in contradiction of this hypothesis. From 0 - 24 h time on stream the expected initial deactivation is observed, but the catalysts are shown to deactivate at different rates. As mentioned, the XPS results indicate that the catalysts undergo a restructuring during operation. The rate of this restructuring appears to depend on the catalyst preparation method, or the initial location of Mn. This in turn can explain the different rates of deactivation. It should also be noted that under the different conversion levels tested, different partial pressures of indigenous water is present which is well established as a cause of deactivation [67, 68].

Fig. 6 shows the selectivity towards $C_{2-4}$ olefins evaluated at various CO conversion levels and temperatures. As the effect CO conversion on the selectivity is known to be significant [33], all reported selectivity values have been evaluated at comparable CO conversion levels (±5%). The light olefin selectivity for the Mn-promoted catalysts is notably higher than for the unpromoted catalyst, caused by a 2-2.5 fold increase in the O/P ratio, as seen in Fig. 7 which shows the $\alpha$-olefin/$n$-paraffin ratio in the gas phase of the product stream. The increase in light olefin selectivity is however lessened by the shift towards a heavier product spectrum, as evidenced by the increase in $C_{5+}$ selectivity, shown in Fig. 8 and simultaneous decrease in $CH_4$, shown in Fig. 9.

The $CH_4$ selectivity displays a negative correlation with CO conversion caused by a shift towards a higher carbon no. product spectrum, agreeing with previous results [33]. The opposite trend is visible for the Co reference catalyst. A review by Yang et al. [69] compiles a list of various Co catalysts and their correlation between conversion and $CH_4$ selectivity, all in disagreement with the observed trend. A similar trend as we find has

however been observed for a Ru catalyst [70], where it was attributed to an increasing rate of hydrogenolysis of olefins producing methane and paraffins. Olefin hydrogenolysis has previously also been observed on Co [71]. The temperature in the present work is above what is conventionally applied so hydrogenolysis may be a possible explanation for our observed trend.

The increased space time also facilitates secondary olefin reactions, as evidenced by the decrease in O/P ratio, this in turn also affects the light olefin and $C_{5+}$ selectivity. Increasing the temperature was shown to have little effect on the light olefin selectivity. The observed decrease in O/P ratio is countered by a shift towards a lighter product yield, shown by the $C_{5+}$ and $CH_4$ selectivity.

The selectivity results for the Mn-promoted catalysts appear to be independent on the catalyst preparation method. The restructuring seen by XPS, particularly the Mn:Co signal ratios, could indicate that the catalyst's structures change towards a similar morphology during operation despite their different original states. The fact that this near identical behaviour is observed already in the earliest stage of the reaction suggests that the restructuring predominantly takes place during the reduction pre-treatment, which was also previously suggested [30].

Previous investigations into the effect of Mn promotion have yielded a range of results. Using co-impregnation of Co and Mn on $TiO_2$, Morales et al. [9, 30] found Mn to strongly interact with the support and have little to no effect on the catalytic performance. No effect on selectivity was found with the Mn→Co and Co→Mn impregnation routes [30] either, however deposition-precipitation of Co and subsequent impregnation of Mn yielded better Co-Mn contact and similar promotion effects as reported here. Using the Co→Mn impregnation route on CNF, Bezemer et al. [55] also found similar results as reported here with little Mn-CNF interaction. Good Co-Mn contact seems to be paramount to obtain a promotion effect from Mn, and the operating state and location of Mn is appears to be less dependent on its initial state, or catalyst preparation method, for $\gamma$-$Al_2O_3$ and CNF supports than for a strongly interacting support like $TiO_2$ on which Co and Mn may segregate.

Dinse et al. [72] studied the effect of Mn:Co ratio with Co-impregnation on $SiO_2$, and while they found a similar promotion effect as reported here. The promoting effect of Mn was found to increase for Mn:Co ratios up to 0.05. No further increase was observed at higher Mn loadings, indicating a saturation of the catalytic sites. It was further found by Johnson et al. [66, 73] that for Mn:Co ratios above 0.1, Mn decorates the $SiO_2$ surface as a spectator species. In our study, the Mn:Co ratio is 0.25, above the threshold value

indicated above [66, 72, 73]. An excess of Mn may explain the identical behaviour between preparation methods. During the restructuring, a fraction of Mn migrates to and saturates the catalytically relevant sites, which end up with similar properties, and due to the excess, the rest remain as spectator species, either as MnO decorating the support, or in a mixed oxide phase with the unreduced cobalt. It is worth noting that the value of this Mn:Co threshold also seems to depend on preparation method and support as Morales et al. [65] found a continuous increase in promotion effects with Mn:Co ratios from 0 to 0.45 using the DP preparation method on $TiO_2$.

### 3.3 DFT Calculations

To better understand the nature of the catalyst-adsorbate interactions, we performed DFT calculations on adsorption and reaction steps on simplified model systems. As Mn was found to affect the intrinsic activity and methane selectivity, the calculations focus on CO dissociation and methane formation. The Mn modified models, shown in Fig. 1, were chosen with Mn at the surface and subsurface as the XPS results indicate Mn enrichment of the catalyst surface region. As mentioned, the probable experimental operating state of Mn is MnO rather than $Mn^{(0)}$ [29] which is used in our calculations. Our XPS results also show the presence of $Mn^{2+}$ which could indicate MnO or a more complex mixed compound containing Mn, but for simplicity, promoters are often modelled as metallic rather than oxidic for these types of calculations [28, 74].

The calculated adsorption energies of relevant species are shown in Table 3. All species preferred adsorption in 3-fold hollow sites on the different model surfaces. From the presented values, it is evident that the presence of Mn has a profound effect on the adsorption energetics of C, H and O. A significant increase in adsorption energy due to the presence of Mn is predicted for all the investigated species except $CH_4$ which is similar for all the surfaces. The effect is strongest for the Mn-terminated surface (MnCo), with changes in the adsorption energies being close to, or in excess of 1 eV, but is still significant on the CoMnCo surface without direct Mn-adsorbate contact. The calculated adsorption energies on clean Co(111) are in reasonable agreement with values found in the literature, but as the majority of previous works have focused on the Co(0001) facet, direct comparison is difficult. A previous direct comparison found Co(0001) to bind these species slightly stronger compared to Co(111) [75]. Experimentally, previous investigations have shown with TPD that Mn promotion increases CO binding energy on Co [66], agreeing with our results, as well as on Fe [76] and Rh [77].

In this work, CO activation and $CH_4$ formation is modelled after the carbide mechanism. In this model, CO dissociates directly into C and O, while methanation and chain-growth takes place by hydrogenation of C and coupling of $CH_2$ monomers. While the exact nature of CO dissociation is highly debated [12], the carbide mechanism still retains some merit, especially for surfaces which bind CO strongly [75]. Furthermore, since this is not a mechanistic study, the carbide mechanism is deemed a suitable model reaction for this work.

As seen in Fig. 10 and Table 4, CO dissociation is clearly more energetically favourable in the presence of Mn with the promoter decreasing both the dissociation barrier and increasing the stability of the dissociated state. The breaking of the strong, triple C-O bond and subsequent monomer formation has been proposed as the rate determining step in FTS [79]. Consequently, this find could help explain the enhanced intrinsic activity observed for the Mn-promoted catalysts. A similar observation has previously been made on Mn modified Rh [80, 81], where it was observed that the addition of Mn increased the binding energies of CO, C and O as well as lowering the dissociation barrier. As here, Mn addition also made the endothermic CO dissociation become exothermic. A similar correlation between increased binding energies and decreased CO dissociation barrier has also previously been observed when comparing dissociation of CO on Co step and terrace sites [18, 82].

The energetics for the stepwise hydrogenation of surface C towards $CH_4$ is illustrated in Fig. 11 and in Table 4. For the first 2 hydrogenation steps, or the monomer formation, there is little difference in the behaviour between the clean Co and Mn modified surfaces. A small increase in the hydrogenation barrier is observed with Mn modification for $CH_2$ hydrogenation. Moreover, the adsorbed $CH_3$ becomes less stable relative to $CH_2$+H on the Mn modified surfaces compared to the pure Co surface. The largest activation barrier is predicted for the final hydrogenation step in methane formation which has also previously been identified as the rate determining step in methane formation [22]. This step also exhibits the largest differences between the Co and Mn modified surfaces, where the activation barrier increases for the latter two surfaces. It can be seen that $CH_3$ hydrogenation is made significantly less energetically favourable in the presence of Mn. The hydrogenation barrier is increased, and a strong relative increase in $CH_3$ binding energy compared to the weakly binding $CH_4$ is observed. This unfavourable effect on $CH_3$ hydrogenation agrees with the experimentally observed methane inhibiting effect of Mn. Another finding explaining the $CH_4$ selectivity effect is the strong relative increase in the adsorption energies for the species binding via a C atom, particularly C and $CH_2$. This may indicate that in the presence of Mn, H is displaced by C-binding species, inhibiting

hydrogenation. An increased surface coverage of C species in the presence of Mn has also been observed experimentally by den Breejen et al. [83] using SSITKA.

Previous works have identified olefin binding energy to be the key descriptor for olefin selectivity. Olefin binding energies have not been evaluated in this work. However, observing the hydrogenation barriers in Fig. 11 and Table 4, it can be seen that while the hydrogenation barriers for C and CH are similar, the barrier for hydrogenation of $CH_2$ is increased, resulting in a net stabilising effect on $CH_2$, precursor to olefins and paraffins. With the possible displacement of hydrogen, this may in turn increase the surface coverage of $CH_2$. Consequently, a possible explanation for the experimentally observed increase in olefin selectivity could be an increased surface coverage of olefin precursors coupled with a decreased rate of hydrogenation. Furthermore, an increased surface coverage of $CH_2$ may also induce C-C coupling. A decreased coverage of H could also inhibit chain termination by hydrogenation. Both these effects offer a possible explanation for the experimentally observed increase in $C_{5+}$ selectivity for the Mn promoted catalyst compared to the Co reference.

## 4 Conclusion

Using different impregnation methods, a series of $\gamma$-$Al_2O_3$ supported Co and CoMn FTS catalysts with the same cobalt loading were prepared. Compared to the Co catalyst, the Mn promoted catalysts displayed a larger intrinsic activity, larger selectivity to light olefins and $C_{5+}$ species, whereas the selectivity to $CH_4$ was considerably lower. Mn was found to be closely associated with Co, and a surface enrichment of Mn was observed during the course of operation. Theoretical investigations suggest that Mn promotion of Co has a stabilising effect on the adsorption of CO, C, H, O, $CH_X$ compared to unpromoted Co. This in turn decreases the CO dissociation barrier, which would explain the higher intrinsic activity. Based on the DFT calculations, the selectivity effect observed for $CH_4$ can be explained by an increased barrier for $CH_4$ formation. The predicted stabilising effect on olefin and paraffin precursors on Mn promoted Co may lead to the increased selectivity towards olefins and $C_{5+}$ species observed experimentally. The selectivity effects were all found to be independent on the catalyst preparation method, which can be attributed to a surplus of Mn saturating the catalytically relevant sites causing similar behaviour. The Co-specific activity differed between the Mn promoted catalysts. This was credited to varying degrees of Mn incorporation in the $Co_3O_4$ lattice, causing different degrees of reduction limiting the available metallic Co surface area.

## Acknowledgements

The Norwegian Research Council is gratefully acknowledged for their financial funding through the Gassmaks programme, contract no. 224968/E30. UNINETT Sigma2 is gratefully acknowledged for providing computational resources through projects NN9336K and NN9355K. Rune Myrstad is thanked for his technical assistance in running the FTS experiments.

## References

[1] N. Nesterenko, J. Aguilhon, P. Bodart, D. Minoux, and J.-P. Dath. In *Zeolites and Zeolite-Like Materials,* B. F. Sels and L. M. Kustov, editors, 189–263. Elsevier, Amsterdam (2016).

[2] H. M. Torres Galvis and K. P. de Jong. *ACS Catal.* **3** (2013) 2130–2149.

[3] H. M. Torres Galvis, J. H. Bitter, C. B. Khare, M. Ruitenbeek, A. I. Dugulan, and K. P. de Jong. *Science*. **335** (2012) 835–838.

[4] D. Das, G. Ravichandran, and D. K. Chakrabarty. *Catal. Today*. **23** (1997) 285–293.

[5] M. Feyzi and A. A. Mirzaei. *J. Fuel Chem. Technol.* **40** (2012) 1435–1443.

[6] A. A. Mirzaei, M. Faizi, and R. Habibpour. *Appl. Catal., A*. **306** (2006) 98–107.

[7] L. Zhong, F. Yu, Y. An, Y. Zhao, Y. Sun, Z. Li, T. Lin, Y. Lin, X. Qi, Y. Dai, L. Gu, J. Hu, S. Jin, Q. Shen, and H. Wang. *Nature*. **538** (2016) 84–87.

[8] F. Morales and B. M. Weckhuysen. *Catalysis*. **19** (2006) 1–40.

[9] F. M. Cano, O. L. J. Gijzeman, F. M. F. de Groot, and B. M. Weckhuysen. *Stud. Surf. Sci. Catal.* **147** (2004) 271–276.

[10] K. Shimura, T. Miyazawa, T. Hanaoka, and S. Hirata. *Appl. Catal., A*. **494** (2015) 1–11.

[11] D. Das, G. Ravichandran, and D. K. Chakrabarty. *Appl. Catal., A*. **131** (1995) 335–345.

[12] J. Cheng, P. Hu, P. Ellis, S. French, G. Kelly, and C. M. Lok. *Top. Catal.* **53** (2010) 326–337.

[13] Y. Qi, J. Yang, D. Chen, and A. Holmen. *Catal. Lett.* **145** (2015) 145–161.

[14] M. C. Valero and P. Raybaud. *Catal. Lett.* **143** (2013) 1–17.

[15] M. Ojeda, R. Nabar, A. U. Nilekar, A. Ishikawa, M. Mavrikakis, and E. Iglesia. *J. Catal.* **272** (2010) 287–297.

[16] J. Cheng, P. Hu, P. Ellis, S. French, G. Kelly, and C. M. Lok. *J. Phys. Chem. C*. **112** (2008) 6082–6086.

[17] Y. Qi, J. Yang, X. Duan, Y.-A. Zhu, D. Chen, and A. Holmen. *Catal. Sci. Technol.* **4** (2014) 3534–3543.

[18] X.-Q. Gong, R. Raval, and P. Hu. *Surf. Sci.* **562** (2004) 247–256.

[19] X.-Q. Gong, R. Raval, and P. Hu. *J. Chem Phys.* **122** (2005) 024711.

[20] J. Cheng, X.-Q. Gong, P. Hu, C. M. Lok, P. Ellis, and S. French. *J. Catal.* **254** (2008) 285–295.

[21] J. Cheng, T. Song, P. Hu, C. M. Lok, P. Ellis, and S. French. *J. Catal.* **255** (2008) 20–28.

[22] J. Cheng, P. Hu, P. Ellis, S. French, G. Kelly, and C. M. Lok. *J. Phys. Chem. C*. **113** (2009) 8858–8863.

[23] J. Yang, Y. Qi, J. Zhu, Y.-A. Zhu, D. Chen, and A. Holmen. *J. Catal.* **308** (2013) 37–49.

[24] Y. Qi, C. Ledesma, J. Yang, X. Duan, Y.-A. Zhu, A. Holmen, and D. Chen. *J. Catal.* **349** (2017) 110–117.

[25] N. Balakrishnan, B. Joseph, and V. R. Bhethanabotla. *Surf. Sci.* **606** (2012) 634–643.

[26] N. Balakrishnan, B. Joseph, and V. R. Bhethanabotla. *Appl. Catal., A*. **462-463** (2013) 107–115.

[27] M. Saeys, K. F. Tan, J. Chang, and A. Borgna. *Ind. Eng. Chem. Res.* **49** (2010) 11098–11100.

[28] J. Cheng, P. Hu, P. Ellis, S. French, G. Kelly, and C. M. Lok. *Surf. Sci.* **603** (2009) 2752–2758.

[29] F. Morales, F. M. F. de Groot, O. L. J. Gijzeman, A. Mens, O. Stephan, and B. M. Weckhuysen. *J. Catal.* **230** (2005) 301–308.

[30] F. Morales, D. Grandjean, A. Mens, F. M. F. de Groot, and B. M. Weckhuysen. *J. Phys. Chem. B*. **110** (2006) 8626–8639.

[31] G. S. Pawley. *J. Appl. Crystallogr.* **14** (1981) 357–361.

[32] Bruker AXS, Karlsruhe, Germany. *TOPAS V4: General profile and structure analysis software for powder diffraction data*, (2008).

[33] S. Storsæter, Ø. Borg, E. A. Blekkan, and A. Holmen. *J. Catal.* **231** (2005) 405–419.

[34] G. Kresse and J. Hafner. *Phys. Rev. B: Condens. Matter*. **47** (1993) 558–561.

[35] G. Kresse and J. Hafner. *Phys. Rev. B: Condens. Matter*. **49** (1994) 14251– 14269.

[36] G. Kresse and J. Furthmüller. *Comput. Mat. Sci.* **6** (1996) 15–50.

[37] G. Kresse and J. Furthmüller. *Phys. Rev. B: Condens. Matter*. **54** (1996) 11169–11186.

[38] J. P. Perdew, K. Burke, and M. Ernzerhof. *Phys. Rev. Lett.* **77** (1996) 3865–3868.

[39] J. P. Perdew, K. Burke, and M. Ernzerhof. *Phys. Rev. Lett.* **78** (1997) 1396.

[40] P. E. Blochl. *Phys. Rev. B: Condens. Matter*. **50** (1994) 17953–17979.

[41] G. Kresse and D. Joubert. *Phys. Rev. B: Condens. Matter*. **59** (1999) 1758–1775.

[42] H. J. Monkhorst and J. D. Pack. *Phys. Rev. B: Condens. Matter*. **13** (1976) 5188–5192.

[43] G. Henkelman and H. Jónsson. *J. Chem Phys.* **113** (2000) 9901–9904.

[44] G. Henkelman and H. Jónsson. *J. Chem Phys.* **113** (2000) 9978–9985.

[45] G. Henkelman and H. Jónsson. *J. Chem Phys.* **111** (1999) 7010–7022.

[46] M. Sadeqzadeh, H. Karaca, O. V. Safonova, P. Fongarland, S. Chambrey, P. Roussel, A. Griboval-Constant, M. Lacroix, D. Curulla-Ferré, F. Luck, and A. Y. Khodakov. *Catal. Today*. **164** (2011) 62–67.

[47] C. P. Gazzara, R. M. Middleton, R. J. Weiss, and E. O. Hall. *Acta Crystallogr.* **22** (1967) 859–862.

[48] *Natl. Bur. Stand. (U.S.) Monogr.* **25-4** (1966) 10.

[49] K. Momma and F. Izumi. *J. Appl. Crystallogr.* **44** (2011) 1272–1276.

[50] Ø. Borg, M. Rønning, S. Storsæter, W. van Beek, and A. Holmen. *Stud. Surf. Sci. Catal.* **163** (2007) 255–272.

[51] F. Morales, F. M. F. de Groot, P. Glatzel, E. Kleimenov, H. Bluhm, M. Hävecker, A. Knop-Gericke, and B. M. Weckhuysen. *J. Phys. Chem. B*. **108** (2004) 16201– 16207.

[52] F. Morales, D. Grandjean, F. M. F. de Groot, O. Stephan, and B. M. Weckhuysen. *Phys. Chem. Chem. Phys*. **7** (2005) 568–572.

[53] M. C. Biesinger, B. P. Payne, A. P. Grosvenor, L. W. M. Lau, A. R. Gerson, and R. S. Smart. *Appl. Surf. Sci.* **257** (2011) 2717–2730.

[54] K. H. Cats, J. C. Andrews, O. Stéphan, K. March, C. Karunakaran, F. Meirer, F. M. F. de Groot, and B. M. Weckhuysen. *Catal. Sci. Technol.* **6** (2016) 4438–4449.

[55] G. L. Bezemer, P. B. Radstake, U. Falke, H. Oosterbeek, H. P. C. E. Kuipers, A. J. van Dillen, and K. P. de Jong. *J. Catal.* **237** (2006) 152–161.

[56] N. E. Tsakoumis, R. Dehghan, R. E. Johnsen, A. Voronov, W. van Beek, J. C. Walmsley, Ø. Borg, E. Rytter, D. Chen, M. Rønning, and A. Holmen. *Catal. Today*. **205** (2013) 86–93.

[57] G. L. Bezemer, U. Falke, A. J. van Dillen, and K. P. de Jong. *Chem. Commun.* (2005) 731–733.

[58] G. L. Bezemer, J. H. Bitter, H. P. C. E. Kuipers, H. Oosterbeek, J. E. Holewijn,

X. Xu, F. Kapteijn, A. J. van Dillen, and K. P. de Jong. *J. Am. Chem. Soc.* **128** (2006) 3956–3964.

[59] Z. Yu, Ø. Borg, D. Chen, B. C. Enger, V. Frøseth, E. Rytter, H. Wigum, and A. Holmen. *Catal. Lett.* **109** (2006) 43–47.

[60] G. L. Bezemer, T. J. Remans, A. P. van Bavel, and A. I. Dugulan. *J. Am. Chem. Soc.* **132** (2010) 8540–8541.

[61] A. M. Saib, D. J. Moodley, I. M. Ciobîcă, M. M. Hauman, B. H. Sigwebela, C. J. Weststrate, J. W. Niemantsverdriet, and J. van de Loosdrecht. *Catal. Today*. **154** (2010) 271–282.

[62] M. M. Hauman, A. Saib, D. J. Moodley, E. du Plessis, M. Claeys, and E. van Steen. *ChemCatChem*. **4** (2012) 1411–1419.

[63] N. E. Tsakoumis, R. E. Johnsen, W. van Beek, M. Rønning, E. Rytter, and A. Holmen. *Chem. Commun.* **52** (2016) 3239–3242.

[64] H. Bordeneuve, C. Tenailleau, S. Guillemet-Fritsch, R. Smith, E. Suard, and A. Rousset. *Solid State Sci.* **12** (2010) 379–386.

[65] F. Morales, E. de Smit, F. M. F. de Groot, T. Visser, and B. M. Weckhuysen. *J. Catal.* **246** (2007) 91–99.

[66] G. R. Johnson, S. Werner, and A. T. Bell. *ACS Catal.* **5** (2015) 5888–5903.

[67] S. Storsæter, Ø. Borg, E. A. Blekkan, B. Tøtdal, and A. Holmen. *Catal. Today*. **100** (2005) 343–347.

[68] N. E. Tsakoumis, M. Rønning, Ø. Borg, E. Rytter, and A. Holmen. *Catal. Today*. **154** (2010) 162–182.

[69] J. Yang, W. Ma, D. Chen, A. Holmen, and B. H. Davis. *Appl. Catal., A*. **470** (2014) 250–260.

[70] R. C. Everson, E. T. Woodburn, and A. R. M. Kirk. *J. Catal.* **53** (1978) 186–197.

[71] E. W. Kuipers, C. Scheper, J. H. Wilson, I. H. Vinkenburg, and H. Oosterbeek. *J. Catal.* **158** (1996) 288–300.

[72] A. Dinse, M. Aigner, M. Ulbrich, G. R. Johnson, and A. T. Bell. *J. Catal.* **288** (2012) 104–114.

[73] G. R. Johnson and A. T. Bell. *J. Catal.* **338** (2016) 250–264.

[74] R. V. Belosludov, S. Sakahara, K. Yajima, S. Takami, M. Kubo, and A. Miyamoto. *Appl. Surf. Sci.* **189** (2002) 245–252.

[75] J.-X. Liu, H.-Y. Su, D.-P. Sun, B.-Y. Zhang, and W.-X. Li. *J. Am. Chem. Soc.* **135** (2013) 16284–16287.

[76] Z. Yang, X. Pan, J. Wang, and X. Bao. *Catal. Today*. **186** (2012) 121–127.

[77] W. Mao, J. Su, Z. Zhang, X.-C. Xu, W. Dai, D. Fu, J. Xu, X. Zhou, and Y.-F. Han. *Chem. Eng. Sci.* **135** (2015) 312–322.

[78] S. Ma, Z. Jiao, X. Zhang, and X. Dai. *Comp. Theor. Chem.* **1009** (2013) 55–59.

[79] G. P. van der Laan and A. A. C. M. Beenackers. *Cat. Rev. - Sci. Eng*. **41** (1999) 255–318.

[80] X. Ma, H. Su, H. Deng, and W.-X. Li. *Catal. Today*. **160** (2011) 228–233.

[81] F. Li, D. Jiang, X. C. Zeng, and Z. Chen. *Nanoscale*. **4** (2012) 1123–1129.

[82] M. A. Petersen, J.-A. van den Berg, I. M. Ciobˆıc˘a, and P. van Helden. *ACS Catal.* **7** (2017) 1984–1992.

[83] J. P. den Breejen, A. M. Frey, J. Yang, A. Holmen, M. M. van Schooneveld, F. M. F. de Groot, O. Stephan, J. H. Bitter, and K. P. de Jong. *Top. Catal.* **54** (2011) 768–777

Table 1: Catalyst characterisation results

| | D [%] | | $d_{Co_3O_4}$[b] | a[b*] | TPR peaks [°C] | | DoR |
|---|---|---|---|---|---|---|---|
| Catalyst | $H_2$[a] | XRD | [nm] | [Å] | $Co_3O_4 \rightarrow CoO$ | $CoO \rightarrow Co^{(0)}$ | [%] |
| Co | 5.5 | 8.1 | 15.8 | 8.0802(7) | 292 | 429 | 87 |
| Co+Mn | 2.2 | 7.3 | 17.6 | 8.0933(7) | 313 | 546 | 60 |
| Co→Mn | 3.4 | 8.4 | 15.3 | 8.0841(7) | 333 | 467 | 79 |
| Mn→Co | 4.6 | 9.1 | 14.1 | 8.0858(8) | 293 | 408 | 84 |

[a)] Measured by $H_2$-chemisorption, [b)] Measured by XRD. [*)] $Co_3O_4$ unit cell parameter.

Table 2: Surface atomic ratios determined using XPS

| | | Atomic Ratio | | | |
|---|---|---|---|---|---|
| Catalyst | State | Mn:Co | Co:Al | Mn:Al | (Co+Mn):Al |
| Co | fresh | - | 0.06 | - | 0.06 |
| Co+Mn | fresh | 0.49 | 0.04 | 0.02 | 0.06 |
| Co→Mn | fresh | 0.97 | 0.02 | 0.01 | 0.03 |
| Mn→Co | fresh | 0.12 | 0.08 | 0.01 | 0.09 |
| Mn | fresh | - | - | 0.31 | 0.31 |
| Co | spent | - | 0.21 | - | 0.21 |
| Co+Mn | spent | 0.65 | 0.12 | 0.08 | 0.20 |
| Co→Mn | spent | 0.99 | 0.06 | 0.06 | 0.13 |
| Mn→Co | spent | 0.61 | 0.12 | 0.08 | 0.20 |

Table 3: Adsorption energies of the main surface species on the Co and Mn-modified Co model surfaces

| Species/ | | $E_{ads}$ [eV] | | |
|---|---|---|---|---|
| surface | Co(111) | Co/Mn/Co(111) | Mn/Co(111) | Literature values |
| CO | -1.76 | -2.13 | -2.55 | -1.61[a], -1.88[b], -1.66[c], -1.43[d] |
| C | -6.95 | -7.43 | -8.15 | -6.80[a], -6.71[b], -6.46[c], -6.54[e], -6.62[f], -7.09[g] |
| O | -5.73 | -6.19 | -7.27 | -5.61[a], -5.43[b], -5.34[c], -5.42[h] |
| H | -2.84 | -3.25 | -3.75 | -2.88[b], -2.72[c], -2.94[f], 2.85[h] |
| CH | -6.42 | -6.83 | -7.55 | -6.31[b], -6.54[e], -5.99[f] |
| $CH_2$ | -4.02 | -4.54 | -5.44 | -3.86[b], -3.86[e], -3.85[f] |
| $CH_3$ | -1.93 | -2.38 | -3.03 | -2.00[e], -1.89[f] |
| $CH_4$ | -0.02 | -0.02 | -0.02 | |

[a)] Co(111), [b–h)] Co(0001). [a)] PBE functional, VASP Code [75], [b)] PW91 functional, DACAPO Code [15], [c)] PW91 functional, CASTEP Code [18], [d)] PBE functional, VASP Code [78], [e)] PBE functional, SIESTA Code [20], [f)] PW91 functional, CASTEP Code [19], [g)] PBE functional, VASP Code [26], [h)] PBE functional, VASP Code [25].

Table 4: Elementary reaction energy barriers on the Co and Mn-modified Co model surfaces

| Elementary reaction/ Surface | $E_a$ [eV] Co(111) | Co/Mn/Co(111) | Mn/Co(111) | Literature values |
|---|---|---|---|---|
| $CO \rightarrow C + O$ | 2.43 | 2.27 | 1.13 | 2.48[a], 3.80[b], 2.70[c] |
| $C + H \rightarrow CH$ | 0.77 | 0.62 | 0.85 | 0.41[b], 0.83[e], 0.85[f] |
| $CH + H \rightarrow CH_2$ | 0.66 | 0.57 | 0.76 | 0.37[b], 0.65[e], 0.66[f] |
| $CH_2 + H \rightarrow CH_3$ | 0.47 | 0.69 | 0.66 | 0.60[e], 0.63[f] |
| $CH_3 + H \rightarrow CH_4$ | 0.82 | 1.06 | 1.26 | 0.96[e], 1.09[f] |

[a)] Co(111), [b)] Co(0001) w/0.5 ML CO, [c–h)] Co(0001). [a)] PBE functional, VASP Code [75], [b)] PW91 functional, DACAPO Code [15], [c)] PW91 functional, CASTEP Code [18], [e)] PBE functional, SIESTA Code [20], [f)] PW91 functional, CASTEP Code [19].

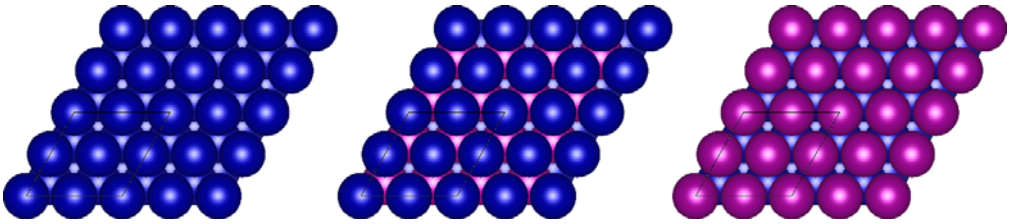

Figure 1: Top view of the different model surfaces used in the calculations. The (2×2) surface unit is outlined. (● = Co, ● = Mn). Visualised using VESTA [49].

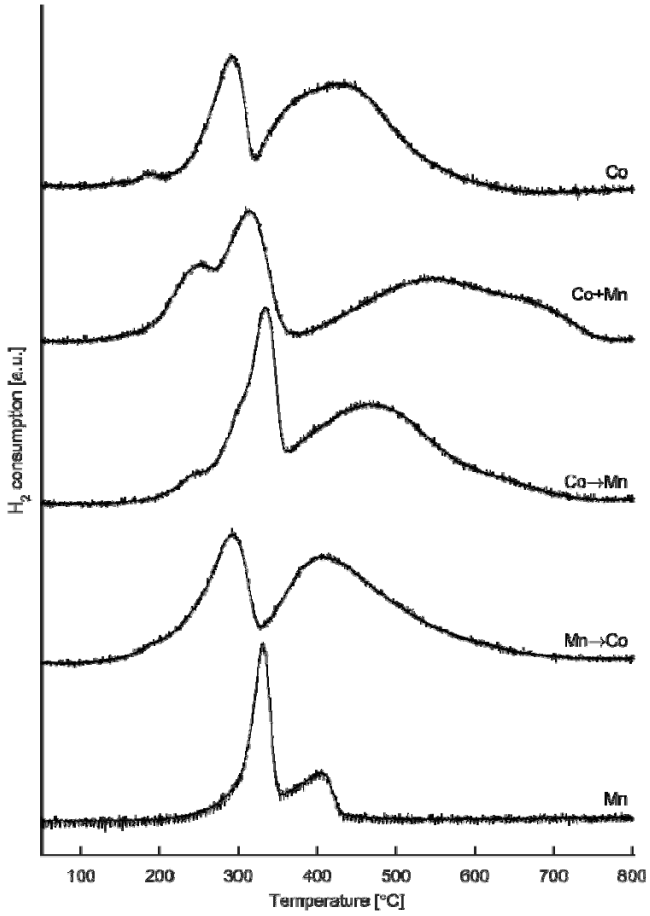


Figure 2: Temperature programmed reduction profiles for $CoMn/Al_2O_3$ catalysts. Reduction conditions: 50 mL/min 10%$H_2$/Ar flow, 800 °C (10 °C/min). Co: Co reference, Co+Mn: Co-impregnated, Co→Mn: Sequentially impregnated, Co first, Mn→Co: Mn first, Mn: Mn reference.

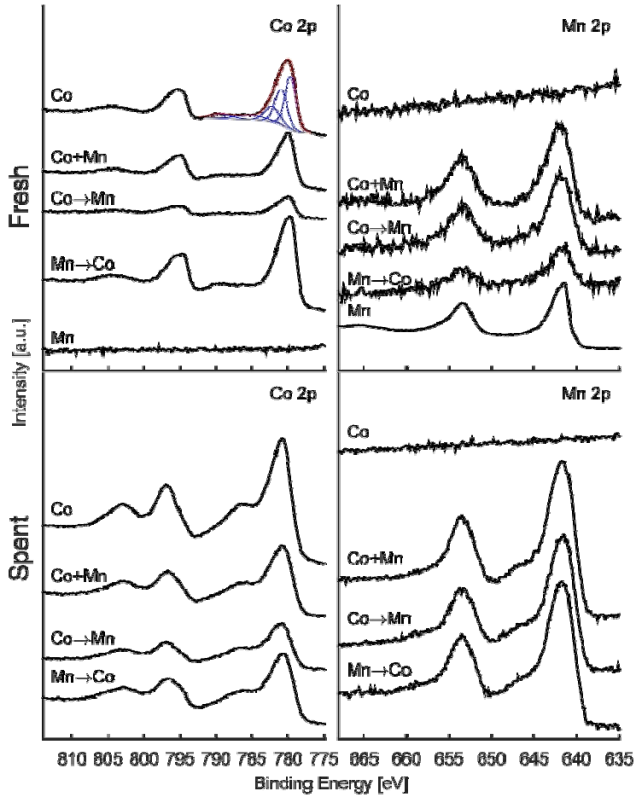


Figure 3: Co 2p (left) and Mn 2p (right) core level spectra of fresh (top) and spent (bottom) catalysts. Co: Co reference, Co+Mn: co-impregnated, Co→Mn: sequentially impregnated, Co first, Mn→Co: Mn first, Mn: Mn reference. The Mn 2p spectrum for the Mn reference catalyst is scaled down ×20.

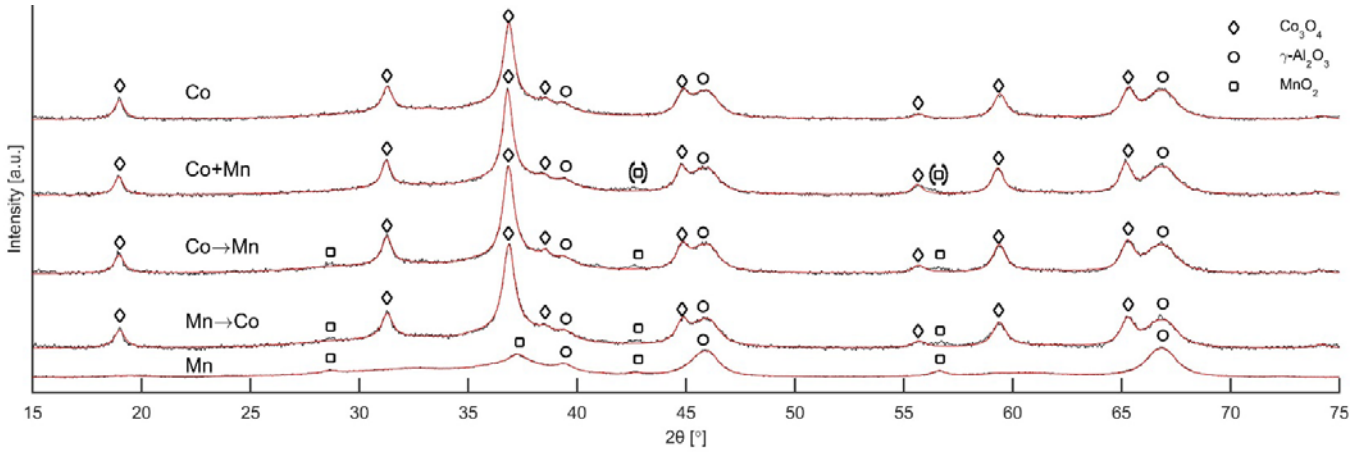


Figure 4: Background subtracted X-ray diffraction patterns (black) and full pattern fits (red) normalised to the γ-$Al_2O_3$ peak at 2θ = 66.9°. Co: Co reference Co+Mn: co-impregnated, Co→Mn: sequentially impregnated, Co first, Mn→Co: Mn first, Mn: Mn reference.

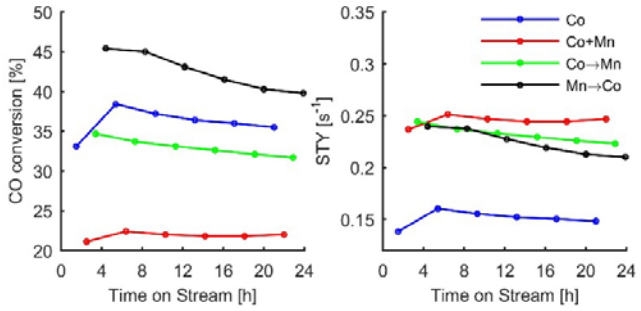


Figure 5: Catalyst conversion (left) and intrinsic activity (right, based on $H_2$ chemisorption) collected at 0-24 h time on stream. Reaction conditions: 15000 NmL/$g_{cat}$·h syngas at $H_2$/CO = 2.1, T = 240 °C, p = 5 bar. Co: Co reference, Co+Mn: Co-impregnated, Co→Mn: Sequentially impregnated, Co first, Mn→Co: Mn first.

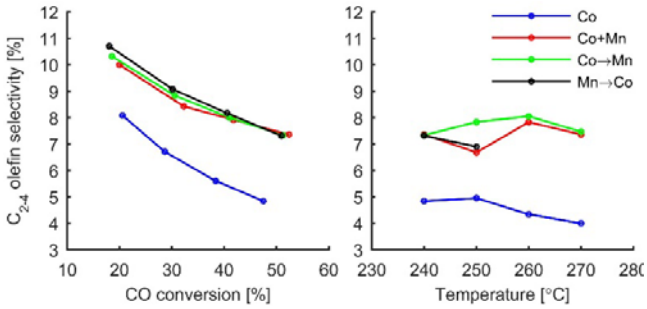


Figure 6: Catalyst selectivity towards $C_2$-$C_4$ olefins evaluated at T = 240 °C and different CO conversion levels (left) and 50 ± 5 % CO conversion and different temperatures (right). Co: Co reference, Co+Mn: Co-impregnated, Co→Mn: Sequentially impregnated, Co first, Mn→Co: Mn first.

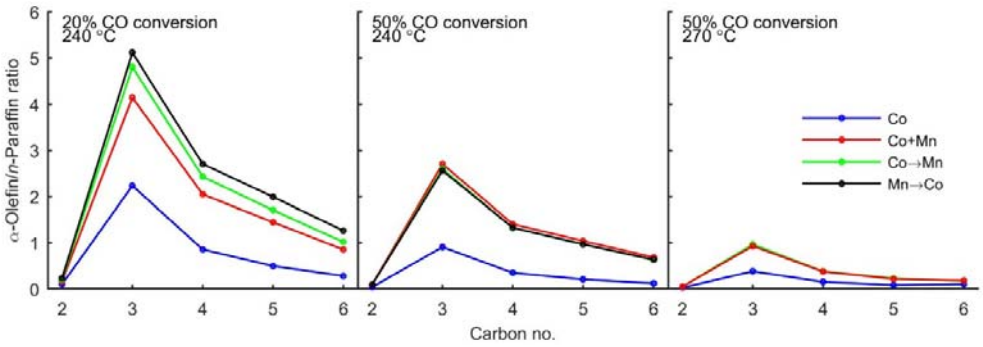


Figure 7: *α*-Olefin/*n*-Paraffin ratio. Co: Co reference, Co+Mn: Co-impregnated, Co→Mn: Sequentially impregnated, Co first, Mn→Co: Mn first.

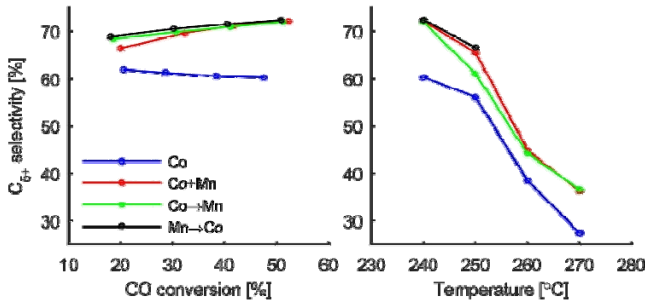


Figure 8: Catalyst selectivity towards C5+ species evaluated at T = 240 °C and different CO conversion levels (left) and 50 ± 5 % CO conversion and different temperatures (right). Co: Co reference, Co+Mn: Co-impregnated, Co→Mn: Sequentially impregnated, Co first, Mn→Co: Mn first.

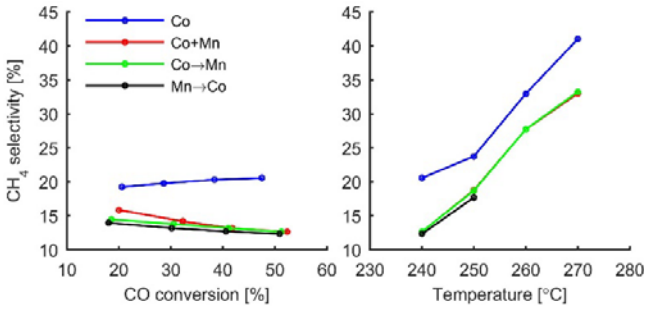


Figure 9: Catalyst selectivity towards $CH_4$ evaluated at T = 240 °C and different CO conversion levels (left) and 50 ± 5 % CO conversion and different temperatures (right). Co: Co reference, Co+Mn: Co-impregnated, Co→Mn: Sequentially impregnated, Co first, Mn→Co: Mn first.

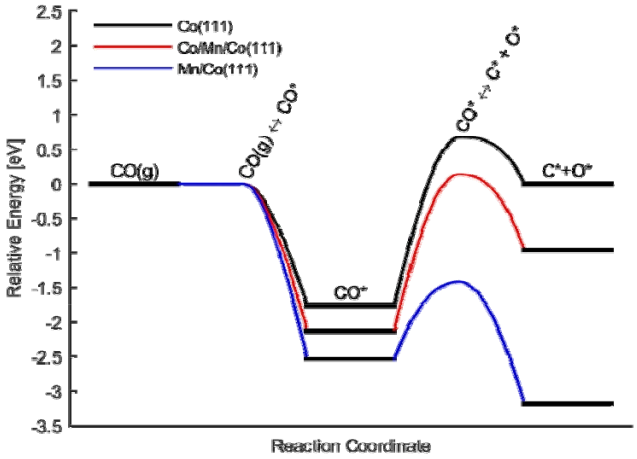


Figure 10: Potential energy diagram for CO adsorption and dissociation on Co and Mn-modified Co model surfaces. Energies shown relative to the clean surface with CO(g).

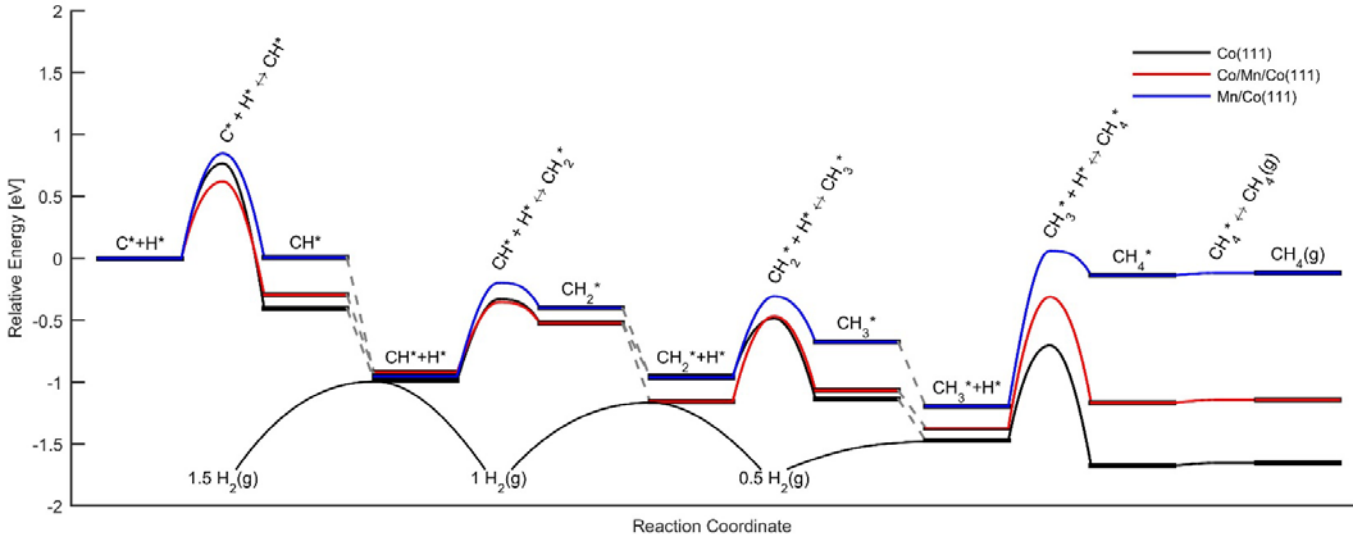


Figure 11: Potential energy diagram for $CH_4$ formation on Co and Mn-modified Co model surfaces. Energies are relative to that adsorbed C* and H* with 1.5 $H_2$ in the gas phase. Grey, dotted lines indicate the energy change due to the adsorption of an additional H.